Development of Many−Body Polarizable Force Fields for Li-Battery Components: 1. Ether, Alkane, and Carbonate-Based Solvents

Oleg Borodin*,† and Grant D. Smith†,‡

Department of Materials Science & Engineering, 122 South Central Campus Drive, Room 304, University of Utah, Salt Lake City, Utah 84112, and Department of Chemical Engineering, University of Utah, Salt Lake City, Utah 84112

Received: September 8, 2005; In Final Form: January 3, 2006

Classical many-body polarizable force fields were developed for *n*-alkanes, perflouroalkanes, polyethers, ketones, and linear and cyclic carbonates on the basis of quantum chemistry dimer energies of model compounds and empirical thermodynamic liquid-state properties. The dependence of the electron correlation contribution to the dimer binding energy on basis-set size and level of theory was investigated as a function of molecular separation for a number of alkane, ether, and ketone dimers. Molecular dynamics (MD) simulations of the force fields accurately predicted structural, dynamic, and transport properties of liquids and unentangled polymer melts. On average, gas-phase dimer binding energies predicted with the force field were between those from MP2/aug-cc-pvDz and MP2/aug-cc-pvTz quantum chemistry calculations.

I. Introduction

Numerous force fields have been developed for simulations of liquids, proteins, amino acids, and polymers over the last 25 years. These force fields can be divided, in general, into three categories: (a) force fields parametrized on the basis of a broad training set of molecules such as small organic molecules, peptides, or amino acids including AMBER,[12−3] COMPASS,[4,5] OPLS-AA,[6] and CHARMM,[7] and a few many-body polarizable force fields;[8−10] (b) generic potentials such as DREIDING[11] and UNIVERSAL[12] that are not parametrized to reproduce properties of any particular set of molecules; and (c) specialized force fields carefully parametrized to reproduce properties of a specific compound such as water,[13,14,15] specific polymers,[16] polymer aqueous solutions,[17] and polymer electrolytes,[18,19] etc.

In choosing a force field for a specific application, care must be taken to ensure that all dominant interactions (electrostatics, polarization, hydrogen bonding, etc) are adequately included, the force field parametrization is performed on compounds of interest or closely related compounds or the force field transferability has been carefully studied, and, finally, the properties of interest were either included in the parametrization of the force field of choice or were shown to be adequately predicted by the force field for similar compounds. For example, a description of thermodynamic properties does not necessarily translate into an adequate prediction of transport properties for liquids and oligomers. Specifically, the OPLS-AA force field parametrized against liquid density, heat of vaporization, and ab initio quantum chemistry-based conformational energetics predicts viscosity of *n*-octane to be 45−100% higher than experiments.[20] A united atom force field designed for the accurate prediction of vapor−liquid equilibrium of perfluoroalkanes predicts a significantly lower (by a factor of 2−5) viscosity of them.[21] Some quantum chemistry-based force fields fail to accurately predict thermodynamic properties, e.g., the Merk MMFF94 force field parametrized on the basis of scaled low-level quantum chemistry data systematically predicts heats of sublimations 30−40% too low[22] for a number of alkane and nonalkane compounds and does not predict a stable *n*-butane liquid at −0.5 °C.[23]

Our goal is to obtain a force field that reliably predicts thermodynamic, structural, and transport properties of electrolytes composed of Li−salts dissolved in nonaqueous liquids, polymer melts, and their combination (gel or plasticized electrolytes) that are aimed, but not limited, to Li−metal and Li−ion battery applications. A key decision we need to make at the beginning of force field development is whether to include solvent polarization explicitly in the force field, through inclusion of dipole polarizability terms, or use computationally inexpensive fluctuating charge or an effective two-body potential. Experience with employing effective two-body force fields for simulating liquids and their interactions with large monovalent cations, such as a K^+ cation,[24] indicates that effective two-body potentials such as OPLS-AA usually adequately predict thermodynamic, structural, and often transport properties of pure liquids and dissociated electrolytes. However, significant deviations of predicted properties are sometimes reported even for pure polar liquids when two-body force fields are utilized. For example, Tasaki[25] reported in a recent simulation study of propylene carbonate (PC) and dimethyl carbonate (DMC) liquids employing a proprietary COMPASS force field room-temperature densities of 1.03 ± 0.01 and 1.03 ± 0.00 g/cm^3 for PC and DMC, respectively, which are 13 and 7% lower than experimental densities of PC and DMC.

Li^+ is a much smaller cation than the K^+ cation. This allows Li^+ to closely approach a solvent and/or an anion and significantly polarize them. Our previous quantum chemistry studies[26,27] of Li^+/anion and Li^+/1,2-dimethoxyethane (DME) interactions indicated that polarization of anions (PF_6^-, BF_4^-) and DME by Li^+ accounts for approximately one-third of the binding energy, thus stressing the need for an accurate representation of polarization effects in the Li^+/anion/solvent force

* To whom correspondence should be addressed. E-mail: borodin@eng.utah.edu.
† Department of Materials Science & Engineering.
‡ Department of Chemical Engineering.

10.1021/jp055079e CCC: $33.50
Published on Web 03/04/2006

field. The importance of the inclusion of water polarization by a Li^+ was also evident from Li^+/water simulation studies,[28] where two-body force fields parametrized based upon $Li^+\cdots H_2O$ dimer energies dramatically overestimated Li^+ energy of hydration and yielded an incorrect coordination number. Although the inclusion of many-body polarizable terms in the force field is the most rigorous approach to incorporating these effects, numerous studies reported using two-body force fields that effectively take solvent polarization into account.[18,19,26−28] Parametrization of such effective two-body force fields is based either on energies for removal of one solvent molecule from a completed Li^+ first-solvation shell obtained from quantum chemistry calculations,[28] as was done for Li^+/water, or by replacing many-body terms with effective two-body polarizable terms in a force field to reproduce lithium coordination from simulations with many-body potentials.[18] Such approaches often accurately reproduce a number of solvent molecules coordinating Li^+ but were found less reliable than many-body force fields in predicting solvation energies and, in our experience, predicted significantly longer Li^+/solvent residence times than simulations employing many-body polarizable force fields.[18]

Previous Polarizable Force Fields. Recent work on the development of robust quantum chemistry-based polarizable force fields for organic molecules[8−10,18,19] and ion/water[29] interactions indicated high accuracy of simulation predictions of structural and thermodynamic properties. These force fields are typically based on heat of vaporization, liquid density, and gas-phase dimer binding energies obtained from ab initio quantum chemistry calculations[8−10,18,19] or symmetry-adapted perturbation theory.[30] Kaminsky et al.[10] determined polarizabilities and most nonbonded parameters for organic liquids on the basis of quantum-chemistry data except for the dispersion parameters, which where determined by fitting heats of vaporization and liquid density. Molecular dynamics (MD) simulations with the resulting force field predicted densities within 5% and heats of vaporizations within 0.5 kcal/mol for a series of small molecules. This approach is similar to our methodology previously used in the development of the many-body polarizable potential for PEO/$LiBF_4$,[19] in which atomic polarizabilities were fitted to reproduce a polarization response due to the 1*e* test charge and nonbonded parameters were reoptimized to fit liquid density, heat of vaporization, and ether dimer binding energies determined using Møller−Plesset second-order perturbation theory (MP2) with the complete basis set extrapolation.

In this work, we extend our previous approach[19] to the development of many-body polarizable force fields for linear oligoethers with the structure $CH_3-((CH_2)_n-O)_m-O-CH_3$ $n = 1-3$ (POM, PEO, and PTMO, respectively),[31] comb-branched polyepoxide ethers (PEPE), PPO, EC, PC, DMC, and GBL (see Table 1 for a list of abbreviations) on the basis of gas-phase dimer energies, liquid densities, heats of vaporization, and alkane self-diffusion coefficients. We will use an atomic dipole polarizable model because it describes the electrostatic response better than the fluctuating charge model.[32,33] MD simulations employing the developed force field are discussed with the emphasis on the ability to reliably predict static structure factors, dielectric loss, ^{13}C NMR spin−lattice relaxation times, and incoherent intermediate structure factors. In the follow-up paper,[34] we report the development of the lithium trifluoromethanesulfonylimide (LiTFSI, or $LiCF_3SO_2NSO_2CF_3$) force field and MD simulations of a number of nonaqueous liquid electrolytes and polymer electrolytes doped with LiTFSI, focusing on the prediction of ion aggregation and transport properties.

TABLE 1: List of Abbreviated Molecular Names Used in This Paper

DME − 1,2-dimethoxyethane $CH_3OCH_2CH_2OCH_3$
DMM − dimethoxymethane $CH_3OCH_2OCH_3$
1,2-DMP − 1,2 dimethoxypropane $CH_3OCH(CH_3)CH_2OCH_3$
1,3-DMP − 1,3 dimethoxypropane $CH_3OCH_2CH_2CH_2OCH_3$
OM_3DMM − $CH_3OCH_2(OCH_2)_3OCH_3$
EC − ethylene carbonate
PC − propylene carbonate
DMC − dimethyl carbonate
GBL − γ-Butyrolactone
DMA − dimethylamine
PEO − poly(ethylene oxide)
POM − poly(oxymethylene)
PTMO − poly(trimethylene oxide)
PPO − poly(propylene oxide)
PEPE − poly(epoxide ether)

II. Force Field Development Methodology

A. Force Field Functional Form. In our classical force field the total potential energy of the ensemble of atoms, represented by the coordinate vector **r**, is denoted as $U^{tot}(\mathbf{r})$. The latter is represented as a sum of nonbonded interactions $U^{NB}(r_{ij})$ as well as energy contributions due to bonds $U^{BOND}(r_{ij})$ having bond length r_{ij}, bends $U^{BEND}(\theta_{ijk})$ having bending angle θ_{ijk} and dihedrals $U^{TORS}(\phi_{ijkl})$ with dihedral angle ϕ_{ijkl} and is given by eq 1

$$U^{tot}(\mathbf{r}) = \sum_{i<j} U^{NB}(r_{ij}) + \sum_{ij} U^{BOND}(r_{ij}) + \sum_{ijk} U^{BEND}(\theta_{ijk}) + \sum_{ijkl} U^{TORS}(\phi_{ijkl}) \quad (1)$$

The nonbonded energy $U^{NB}(\mathbf{r})$ consists of a sum of the two-body repulsion and dispersion energy $U^{RD}(\mathbf{r})$, the energy due to multipole−multipole (charge−charge, charge−dipole, etc) interactions (Coulomb) and a potential energy due to polarization U^{pol}

$$U^{NB}(\mathbf{r}) = U^{RD}(\mathbf{r}) + U^{coul}(\mathbf{r}) + U^{pol}(\mathbf{r}) \quad (2)$$

The Coulomb interactions are represented in liquids by assigning partial charges (q_i, q_j) to atomic centers and off-atom sites (eq 3)

$$U^{coul}(\mathbf{r}) = \frac{1}{2}\sum_i \sum_j \frac{q_i q_j}{4\pi\epsilon_0 r_{ij}} \quad (3)$$

where ϵ_0 is dielectric permittivity of vacuum. In accord with Kaminsky et al.,[8] we found that the addition of an off-atom site is needed to improve the electrostatic potential description near electron lone-pairs. However, instead of introducing two additional force centers to model the lone-pair contribution to the electrostatic potential around ether oxygen atoms, we used a single "extended charge" that was situated at 0.5 Å from the oxygen atom, as shown in Figure 1.[35] We also noticed that

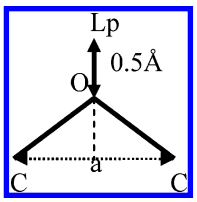

Figure 1. Location of the "extended charge" at ether oxygen atoms. The "extended partial charge" denoted as Lp is located at the continuation of the O−*a* median.

inclusion of the lone-pairs on the N atom (in $TFSI^-$ anion) did not significantly improve the description of the electrostatic potential around $TFSI^-$; therefore, no additional off-site atoms were added to model the lone-pair contribution to electrostatic potential near nitrogen atoms.

The atom dipole polarizability model is used to represent many-body polarizable interaction in our force field. To prevent a "polarization catastrophe" from occurring at close atom approaches, the induced dipole−induced dipole interactions were damped using the modified Thole[36] model, in which induced dipoles are damped as though one of the point dipoles in each pairwise interaction is replaced by a smeared charge distribution. In the atomic polarizability model, the potential energy due to dipole polarization is not pairwise additive and is given by eq 4−5 using the Ponder's notation for damping functions, given by eq 5−8,[37]

$$U^{\mathrm{pol}}(\mathbf{r}) = -\sum_i \mu_i \cdot \boldsymbol{E}_i^0 - 0.5 \sum_i \sum_j \mu_i \cdot \boldsymbol{T} \cdot \mu_j + \sum_i (\mu_i \cdot \mu_i / 2\alpha_i) = -0.5 \sum_i \mu_i \cdot \boldsymbol{E}_i^0 \quad (4)$$

where $\mu_i = \alpha_i \boldsymbol{E}_{\mathrm{tot}}$, α_i is the isotropic atomic polarizability fitted to reproduce polarization response of a molecule due to a test charge, $\boldsymbol{E}_{\mathrm{tot}}$ is the total electrostatic field at the atomic site i due to permanent charges and induced dipoles, $\boldsymbol{E}_i^0$ is the electrostatic field due to permanent charges only, and the second-order dipole tensor $\boldsymbol{T}_{ij}$ is given by

$$\boldsymbol{T}_{ij} = \frac{1}{4\pi\epsilon 0 r_{ij}^3}\left[\lambda_5(r_{ij})\frac{3\mathbf{r}_{ij}\mathbf{r}_{ij}}{r_{ij}^2} - \lambda_3(r_{ij})\right] \quad (5)$$

$$\lambda_5(r_{ij}) = 1 - (1 + a_{\mathrm{T}}u^3)\exp(-a_{\mathrm{T}}u^3) \quad (6)$$

$$\lambda_3(r_{ij}) = 1 - \exp(-a_{\mathrm{T}}u^3) \quad (7)$$

$$u = r_{ij}/(\alpha_i\alpha_j)^{1/6} \quad (8)$$

The Thole screening parameter a_{T} defining the width of the smeared charge distribution was set to 0.4, similar to values used in the polarizable water simulations, 0.39.[37] Atoms connected by bonds and bends were excluded from a list of nonbonded interactions. The interaction between an induced dipole and a partial charge separated by three bonds was scaled by 0.8, because it provided improved description of electrostatic potential around molecules. Due to the exclusion of these closely placed atoms from the list of nonbonded interactions, the interaction energies were rather insensitive to the value of the a_{T} parameter; nevertheless, we decided to include screening of the induced dipole−induced dipole interactions at short distances to improve the stability of our simulations.

The contributions due to bends $U^{\mathrm{BEND}}(\theta_{ijk})$ and torsions $U^{\mathrm{TORS}}(\phi_{ijkl})$ for atoms i, j, k, and l having atom types α, β, γ, and δ, respectively, are given by

$$U^{\mathrm{BEND}}(\theta_{ijk}) = {}^1/_2\, k_{\alpha\beta\gamma}{}^{\mathrm{BEND}}(\theta_{ijk} - \theta^0_{\alpha\beta\gamma})^2 \quad (9)$$

$$U^{\mathrm{TORS}}(\phi_{ijkl}) = \sum_n {}^1/_2\, k^{\mathrm{t}}_{\alpha\beta\gamma\delta}(n)[1 - \cos(n\phi_{ijkl})] \quad (10)$$

where $\theta^0_{\alpha\beta\gamma}$ is the equilibrium bend angle for bend type α, β, γ; ϕ_{ijkl} is the dihedral angle of the $\alpha\beta\gamma\delta$ type; $k_{\alpha\beta\gamma}{}^{\mathrm{BEND}}$ and $k^{\mathrm{t}}{}_{\alpha\beta\gamma\delta}(n)$ are the bend force constant and torsional parameters, respectively. Bond lengths were constrained in all simulations.

B. Force Field Fitting Methodology. As in our previous work,[19] we begin force field development with determining atomic polarizabilities by fitting the polarization response of a molecule to a test charge followed by fitting partial charges to obtain the best description of the electrostatic potential around a molecule. Next, the repulsion−dispersion contribution to the nonbonded energy is determined followed by fitting bonding and bending parameters to vibrational frequencies and equilibrium geometries of model compounds. The torsional parameters are fit to obtain the best description of conformational energetics of model compounds obtained from ab initio quantum chemistry calculations.

Fitting repulsion−dispersion interactions is the most challenging and controversial part of force field development because the repulsion−dispersion parameters can be obtained by fitting a number of different data sets yielding somewhat different potentials. The most often used data for fitting the repulsion−dispersion parameters are: crystal structures together with sublimation energies, liquid densities and heats of vaporization, vapor−liquid equilibrium data, static and dynamics structure factors, and gas-phase dimer binding energies obtained from quantum chemistry calculations or from the symmetry-adapted perturbation theory quantum chemistry calculations. Unfortunately, an accurate description of one property does not necessarily translate into accurate predictions of the other properties, as discussed in the Introduction. Fitting to quantum chemistry data, on the other hand, presents a unique opportunity to sample molecular interactions for all molecular approaches and, hence, provide data about intermolecular interactions, e.g., London forces, electrostatic, hydrogen bonding, etc. Quantum chemistry-based force fields based upon sufficiently accurate levels of theory should, in principle, be able to accurately predict all properties.

To develop an accurate quantum chemistry-based force field, one needs to use an adequate functional form of potential energy function, a proper set of combining rules (if any), and, most importantly, an adequate level of theory (basis sets and electron correlation treatment). There is some controversy in the literature as to what level of theory is adequate for fitting force fields, particularly in regards to dispersion interactions. Benchmark calculations performed on noble gases[38] showed that calculations should be performed at the CCSD(T) or at least the MP4 level, and it was necessary to utilize basis sets as large as aug-cc-pvQz. Others[10] argued that cc-pvXz (X = D, T, Q) basis sets should not be augmented with additional sets of diffuse and polarization functions because the use of the gas-phase molecular polarizability from aug-cc-pvXz basis sets in liquid simulations results in excessive dielectric constant and heat of vaporization of liquids. Therefore, Kaminsky et al.[10] consistently used complete basis set extrapolation for the cc-pvXz basis sets without augmentation at the local pseudo-spectral MP2 (LMP2) level to obtain and fit dimer energies at the most optimal geometries calculated at the LMP2/6-31G* level. Bordner et al.[22] used another strategy, i.e., including a double set of diffusion and polarization functions into the cc-pvDz basis sets (e.g., d-aug-cc-pvDz basis sets) and showed that nonbonded parameters determined by fitting dimer energies at the MP2/d-aug-cc-pvDz level yielded accurate crystal structures and sublimation energies without extrapolating to the complete basis set limit.

Rather then developing a purely quantum chemistry-based force field and validating it against thermodynamic and transport properties of liquids, we have chosen a different strategy. We fit the force field repulsion−dispersion parameters to dimer

energies from rather inexpensive MP2/aug-cc-pvDz calculations as a function of molecular separation and performed minor adjustments to the well depth (ϵ) and its position (r^*) for pair interactions to achieve the optimal fit to liquid densities, heats of vaporization, and in some cases small molecule self-diffusion coefficients. Then we examined which level of theory yielded the best agreement with the developed semiempirical force field.

A modified exp-6 potential was adopted for description of repulsion−dispersion interactions

$$U^{RD} = A\exp(-Br_{ij}) - Cr_{ij}^{\ 6} + D\left(\frac{12}{Br_{ij}}\right)^{12} \qquad (11)$$

The A, B, and C parameters could be expressed in terms of potential well depth ϵ, the interatomic separation at the minimum r^*, and the steepness parameter λ, as given by eq 12

$$A = 6\epsilon(\exp\lambda)/(\lambda - 6) \qquad (12a)$$

$$B = \lambda/r^* \qquad (12b)$$

$$C = \epsilon\lambda(r^*)^6/(\lambda - 6) \qquad (12c)$$

The exp-6 form provides a better fit to dimer energetics calculated from quantum chemistry than the 12−6 Lennard-Jones potential.[39] The term $D^*(12/(B^*r_{ij}))$,[12] $D = 0.0005$ kcal/mol is essentially zero at $r_{ij} \geq r^*$ but becomes the dominant term at $r_{ij} < 1$ Å, ensuring that U^{RD} is repulsive at unphysical close atom approaches.

Our desire to perform empirical adjustments instigates us to use combining rules for nonbonded parmeters to reduce the number of independent parameters. A number of combining rules have been suggested that range from simple arithmetic and geometric means to more complicated forms such as the Waldman−Hagler (WH) combining rule that incorporates van der Waals radii in expressions for combining well depth. The original WH combining rules are given by

$$r^*_{ij} = \left(\frac{r^*_{ii}{}^6 + r^*_{jj}{}^6}{2}\right)^{1/6} \qquad (13a)$$

$$\epsilon_{ij} = 2\left(\frac{r^*_{ii}{}^3 r^*_{jj}{}^3}{r^*_{ii}{}^6 + r^*_{jj}{}^6}\right)\sqrt{\epsilon_{ii}\epsilon_{jj}} \qquad (13b)$$

WH combining rules describe the interaction of noble gases best,[40] and they were also found to be able to describe thermodynamic properties of the CH_4/CF_4 mixtures although other simple combining rules failed to do it.[41] The usage of the WH combining rules gave an appreciably more accurate description of 136 crystal structures and 34 sublimation energies than the arithmetic-geometric for r^* and ϵ combining rules.[42] Thus, we adopted WH combining rules for exp-6 potential, as given by

$$A_{ij} = \sqrt{A_{ii}A_{jj}}\,\frac{B_{ij}^{\ 6}}{B_{ii}^{\ 3}B_{jj}^{\ 3}}$$

$$B_{ij} = \left(\frac{2}{B_{ii}^{\ -6} + B_{jj}^{\ -6}}\right)^{1/6}$$

$$C_{ij} = \sqrt{C_{ii}C_{jj}} \qquad (14)$$

which corresponds to the original WH combining rules[43] when $\lambda_{ii} = \lambda_{jj}$.

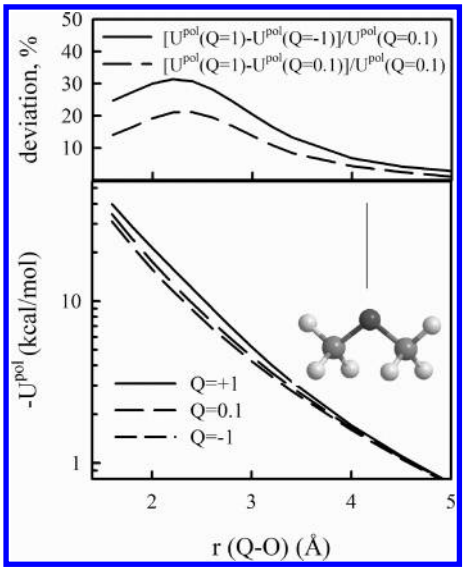

Figure 2. Polarization energy of the dimethyl ether interacting with a test charge.

Bond lengths were constrained to the averages of bond length obtained at the B3LYP/aug-cc-pvDz or MP2/aug-cc-pvDz levels. The equilibrium bend angles (eq 9) were fit to geometries obtained typically at the B3LYP/aug-cc-pvDz and MP2/aug-cc-pvDz levels, whereas torsional parameters (eq 10) were fit to the relative conformational energies and barriers between them determined using MP2/aug-cc-pvDz energies at geometries optimized at the MP2 or B3LYP levels using the aug-cc-pvDz basis set with only a few exceptions, as noted in the text.

III. Quantum Chemistry Calculations and Force Field Development

Four types of quantum chemistry calculations were performed: (a) polarization energy of a molecule interacting with a test charge; (b) electrostatic potential on a grid of points around isolated molecules; (c) dimer binding energies; (d) relative conformational energies and barriers between them. These calculations will be used to obtain the following contributions into the force field: (a) atomic dipole polarizabilities; (b) partial charges; (c) repulsion−dispersion parameters; (d) torsional parameters. Gaussian 98 was used for all calculations.[44]

A. Polarization Energy. Benchmark calculations[45] of molecular polarizability on more than 20 organic compounds + water revealed that the B3LYP/aug-cc-pvDz//MP2(fc)/6-31G-(d) level accurately predicts molecular polarizability in a gas phase. The predicted polarizability at the level was an average of 1% higher than those of experiments with a standard deviation (SD) of 6%. Thus, we adopted the B3LYP/aug-cc-pvDz level for the estimation of polarizable energy using quantum chemistry calculations. A representative plot of the polarization energy due to positive and negative charges located along the paths around a dimethyl ether is shown in Figure 2. Polarization energies due to positive and negative charges are different by up to 30%, with the largest difference observed close to the most probable location of a Li^+ cation in electrolytes, i.e., around 1.8−2 Å from ether oxygen. The dependence of the polarization energy on the charge magnitude and sign arises from a shift of electronic clouds toward a positive test charge and away from a negative test charge. The shift of electronic clouds results in a deviation from the linear response behavior. The larger the magnitude of the test charge, the larger the shift and the larger the deviation from a linear response theory.

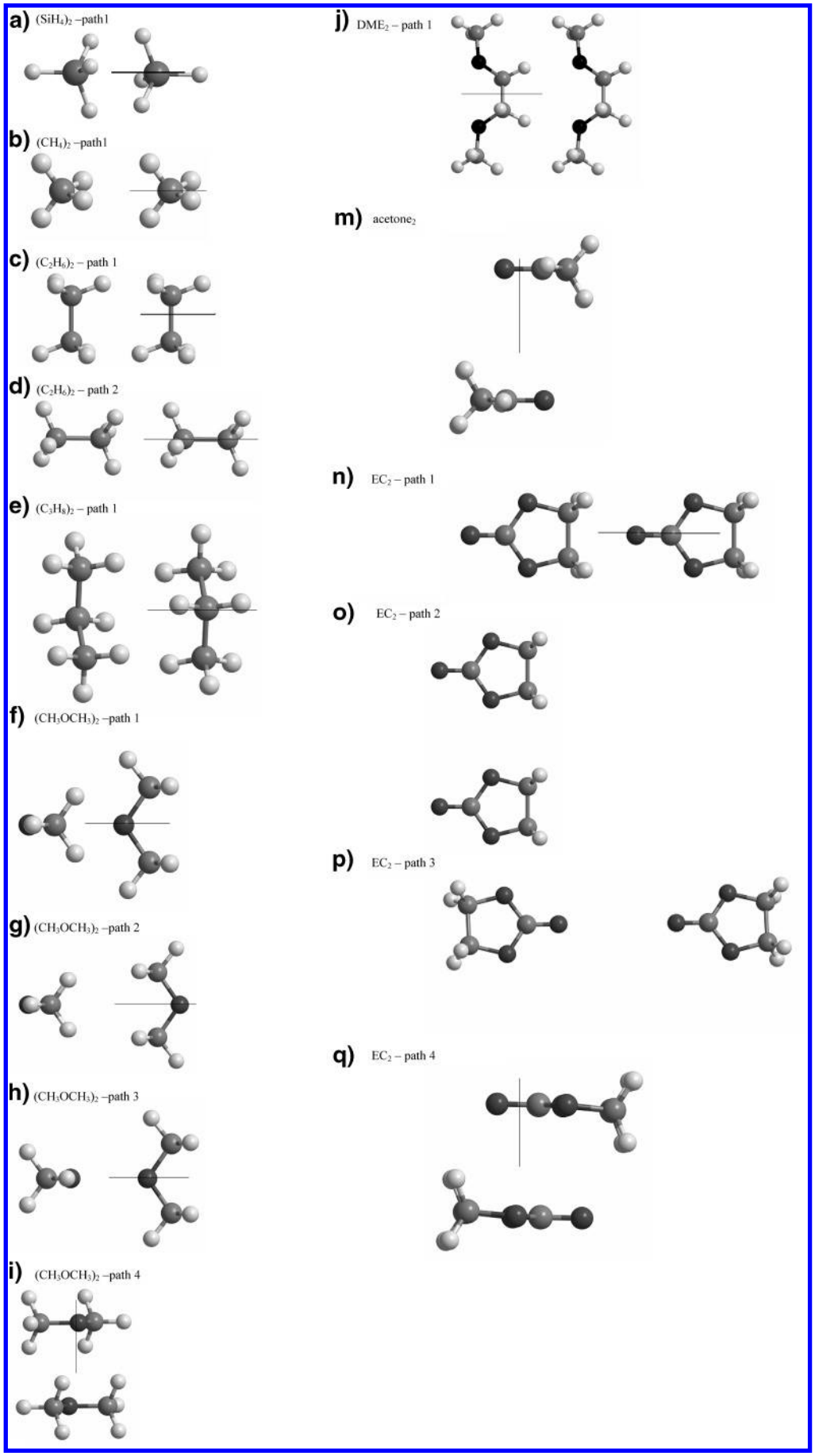

Figure 3. Schematic depiction of the paths used for calculation of the dimer energetics as a function of separation.

Dependence of molecular polarization on the test charge magnitude is absent from the force field (eq 4−8) because the force field form is based on a linear response theory. Figure 2 indicates that the polarization response of dimethyl ether due to a closely approaching Li^+ cation will be underestimated by the force field by ∼10−15% if atomic polarizabilities are parametrized on the basis of interactions with an infinitely small charge. To effectively model polarization response due to a Li^+ cation, we use a positive test charge +1e to fit molecular polarization response in the areas with likely Li^+ coordination, whereas in locations where anion is expected to be present in simulations, a negative −1*e* charge is used to obtain polarization response. The polarization energy due to a test charge +1*e* and −1*e* was calculated for C_2H_6, C_3H_8, C_4F_{10}, dimethyl ether, DME (tgt conformer only), acetone, EC, GBL, and DMC and used to fit atomic polarizabilities. After an initial set of atomic polarizabilities was obtained by fitting polarization energy due to a test charge, the oxygen polarizability was adjusted within 0.2 Å^3 to obtain the best fit to the total solvent/Li^+ binding energy, as described in the follow-up paper.[34]

B. Electrostatic Potential Calculations. Geometry optimization was performed at the MP2/aug-cc-pvDz level for C_2H_6, C_3H_8, CF_4, dimethyl ether, DME (ttt, tgt, ttg, tgg, and tg^+g^- conformers), EC, DMC, GBL, and acetone. The electrostatic potential and the molecular dipole and quadrupole moments were calculated at the MP2/aug-cc-pvDz level at optimized geometries and used to fit partial charges. Charges for atoms with similar chemical environments were transferred from the previously fitted compounds if the transfer did not significantly (10−30%) degrade the fit to the electrostatic potential and its moments. Charges were fit in the following order: (1) combined fit to *n*-alkanes and ethers; (2) cyclic carbonates; (3) linear carbonates; (4) other compounds such as amines, fluoroalkanes, etc.

C. Dimer Binding Energies. Our strategy for developing the repulsion−dispersion parameters is: first, fit them to dimer binding energies calculated at the MP2/aug-cc-pvDz level; second, make empirical adjustments to obtain the best fits to condensed phase experimental data; and third, compare the dimer binding energies from the molecular mechanics (MM) calculations using empirically adjusted repulsion−dispersion parameters with the binding energies from quantum chemistry calculations performed at various levels to identify the level that yields best agreement with the empirically corrected force field.

The Hartree−Fock (HF), MP2, and MP4 level calculations using a family of aug-cc-pvXz (X = D, T, Q) basis sets were performed on a number of dimers shown in Figure 3. Dimer geometries were optimized at the B3LYP/aug-cc-pvDz level, followed by shifting one of the molecules as shown in Figure 3 without geometry optimization. The binding energy was calculated as the energy of a dimer minus a sum of energies of individual molecules at the geometry from the dimer configuration. All energies were corrected for basis set superposition error using the counterpoise method. The HF contribution to the binding energy was found to be insensitive to the basis set size, essentially converging at the aug-cc-pvDz basis set, whereas the electron correlation contribution to the binding energy is evidently dependent on the basis set size. The correlation energy $U_{corr}^{MP2} = U_{MP2} - U_{HF}$ revealed $\sim X^{-3}$ scaling (X = 2, 3, 4 for D, T, Q) for aug-cc-pvXz basis set shown in Figure 4, in agreement with previous reports.[46,47] The existence of one such parameter extrapolation allows rather inexpensive extrapolation to the complete basis set (CBS) limit

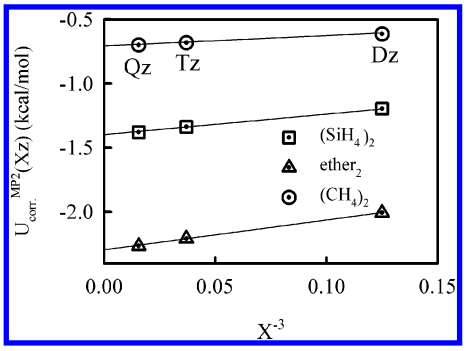

Figure 4. Correlation energy (MP2-HF) as a function of a basis-set size for aug-cc-pvXz, X = D, T, Q, basis sets for SiH_4, CH_4, and CH_3-OCH_3 dimers, respectively.

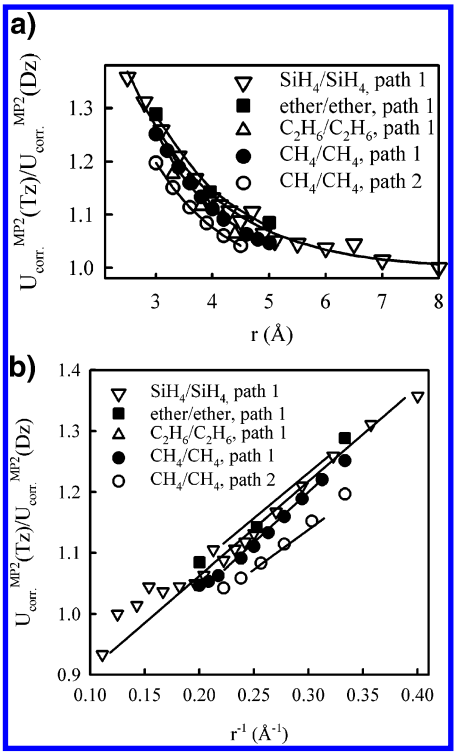

Figure 5. Ratio of the correlation energy (MP2-HF) calculated using aug-cc-pvTz and aug-cc-pvDz basis sets as a function molecular separation. Solid lines are the fits with the (a) C1*exp(−C_2*r)+1 and (b) C_3+C_4/r functions.

using calculations with aug-cc-pvDz and aug-cc-pvTz basis sets only. MP2/CBS extrapolated energies for short alkane and ether dimer from this extrapolation scheme are within a few percent of the CBS extrapolated binding energy obtained by extrapolating correlation energy calculated with cc-pvTz and cc-pvQz basis sets using the procedure from ref 8. This agreement indicates that the MP2/CBS energies are very similar for augmented and nonaugmented cc-pvXz basis sets.

Instead of calculating dimer binding energies for all points along paths of interest using more expensive aug-cc-pvTz basis sets we want to find a reliable interpolation function to fit the U_{corr}^{MP2}(Tz)/ U_{corr}^{MP2}(Dz) ratio, where Tz and Dz denote aug-cc-pvTz and aug-cc-pvDz basis sets. The U_{corr}^{MP2}(Tz)/U_{corr}^{MP2}(Dz) ratio for a number of complexes is shown in Figure 5. It increases as separation between molecules in a dimer decreases. Two empirical functions containing two constants C_1*exp(−C_2*r)+1 (Figure 5a) and C_3+C_4/r (Figure 5 b) fit data well despite having different limiting behavior at large separations. The C_1*exp(−C_2*r)+1 function will be used in this work to

TABLE 2: Liquid Density (ρ), Heat of Vaporization (ΔH), and Self-Diffusion Coefficient (D) and Finite Size Correction to Self-Diffusion Coefficient from MD (ΔDFSC) (see eq a11 in Appendix); All Data Are for Liquids at 1 Atm unless Noted Otherwise; Experimental Data Are Given in Parentheses

liquid	T (K)	run length (ns)	ρ (kg m^{-3})	error ρ (%)	ΔH (kcal/mol)	error ΔH (%)	$D^{MD} + D^{FSC}$ (10^{-10} m s^{-1})	error ($D^{MD} - D^{exp}$)/D^{exp} (%)	ref to exp data
Uncharged Nonpolarizable Force Field									
C_2H_6	184.5	2.0	545 (546)	−0.2	3.31 (3.51)	−6	48.3 + 6.2 (50) [a]	−3	68,69,70
C_3H_8	321.1	2.0	581 (580)	0.2	4.26 (4.55)	−6	48.4 + 6.9 (54.7)	−12	68,71,70
C_3H_8 at 250 MPa	243	2.0	592				45.3 (51.3)	−12	70
C_5H_{12}	298.2	1.5	611 (621)	−1.6	6.15 (6.393)	−4	51.4 + 10.1 (56.2)	−9	72,71,73
$C_{10}H_{22}$	298.2	1.5	725 (727)	−0.3	11.79 (12.28)	−3	11.7 + 2.5 (14)	−16	74,71,75
Many-Body Polarizable Force Field									
C_2H_6	184.5	2.0	560 (546)	2.5	3.31 (3.51)	−4	39.0 + 6.2 (50)[a]	−22	76,77,78
C_3H_8	321.1	2.0	574 (580)	−1.0	4.07 (4.55)	−9	50.3 + 6.9 (54.7)	−8	68,71,70
$C_{10}H_{22}$	298.2	1.5	720 (727)	−0.7	11.24 (12.28)	−8	13.0 + 2.5 (14)	−7	74,71,75
C_4F_{10}	273.2	2.0	1603 (1600)	0.2	5.54 (5.46)	2	23 + 4.6		
C_6F_{14}	298.2	5.0	1660 (1675)	−0.9	7.56 (7.51)	1	17.8 + 2.3		51
C_9F_{20}	295.0	2.0	1784 (1769)	0.8			6.8+1.5		51
dimethyl ether	253.1	1.7	723 (728)	−0.8	4.88 (5.05)	−3	52.5 + 10.2 (53.7)[a]	−2	79,71,80
DME	298.2	17	850 (862)	−1.3	8.70 (8.717)	0	25.5 + 5.9		81,71
DME	303.2	1.5	841		8.46		28 + 6.2 (31.5)	−11	82
diglyme	298.2	0.8	940 (938.9)	0	12.97				83
diglyme	303.2	2.5	930				10.3 + 2.6 (13)	−20	82
diglyme	435.0	1.0	765	9.84 (8.6,10.0)					84,85
triglyme	298.2	3.2	981 (981)	0			3.4 + 1.2		83
triglyme	303.2	4.0	976				4.0 + 1.3 (6.1)	−34	82
DMM	298.2	0.3	850 (857)	−0.8	6.90 (6.904)	0	32.6		86,87
OM_3DMM	298.2	0.3	1052 (1067)	−1.4					88
acetone	298.2	4.0	805 (785)	2.5	7.17 (7.474)	−4	40.9 + 6.7 (37.5−40.9)		89,71,89
EC	313.2	9.0	1302 (1321)	−1.5	14.4		6.9 + 1.4 (8.0)	−13	74, 82
EC	423.2	0.3	1182		12.96 (13.45)	−4	26.5		90
PC	303	14	1206 (1195)	1.1	14.2		4.8 + 1.0 (5.8)	−17	91,82
PC	323	1.0	1185						
PC	423	0.7	1073		12.34 (13.19)	−6	27.1		90
DMC	303	12	1060 (1063)	0.3	9.25 (8.97)	3	18.5 + 2.8 (26)	−29	92,92,82
GBL	303	17	1101 (1118.8)	−1.55	12.32 (12.72)	−3	8.4 + 1.5 (9.0)	−7	93,82,94
DMA	273.2	0.2	690 (680)	1.5	5.93 (6.13)	−7	43 + 6.9		74,71
SO_2	223.2	0.3	1541 (1557)	−1.0	6.25 (6.51)	−4	20.1		95,95

[a] Experimental value at 1 atm pressure was extrapolated using high-pressure data.

interpolate the MP2/aug-cc-pvTz values for intermediate separations. Interestingly, the U_{corr}^{MP2}(Tz)/U_{corr}^{MP2}(Dz) ratio is around 1.1 (±0.03%) at molecular separations corresponding to the minimum energy for complexes shown in Figure 5.

The effect of electron correlation treatment beyond MP2 level was investigated for the aug-cc-pvDz basis set and is shown in Figure 6. The correlation energy U_{corr}^{MP4}(Dz) is larger than U_{corr}^{MP2}(Dz) only by 5% (±3%) at the optimized dimer geom-

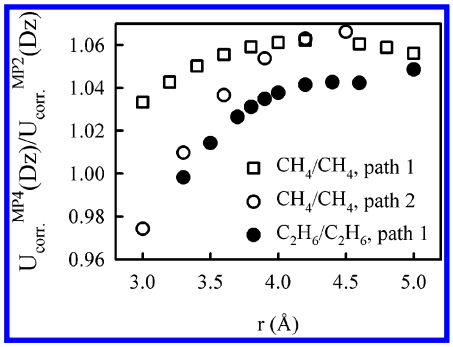

Figure 6. The ratio of (MP4-HF)/(MP2-HF) energies calculated using aug-cc-pvDz basis set.

TABLE 3: Repulsion−Dispersion Parameters[a]

atom type	A (kcal mol^{-1})	B (Å^{-1})	C (kcal mol^{-1} Å^{-6})
H	15480.0	4.8165	29.46
C (generic)	165734.9	3.8867	332.40
C_m in (C_mH_3−O−)	165734.9	3.8867	375.00
C_c in (in carbonyl group)	39080.0	3.9000	500.00
N	25900.0	3.4050	620.00
O	48833.0	3.8236	310.00
F	9693.8	3.5861	164.20
S	95900.0	3.4013	1304.00

[a] To obtain repulsion−dispersion parameters for the uncharged alkane force field, A and C coefficients for hydrogen and carbon atoms should be divided by 1.05.

etries and decreases when molecules approach closely each other. Superposition of electron correlations and basis size contributions into the binding energy (eq 15) was found to be a good approximation,[48]

$$U_{corr}^{MP4}(Tz) = U_{corr}^{MP2}(Dz) * [U_{corr}^{MP4}(Dz)/ U_{corr}^{MP2}(Dz)]* [U_{corr}^{MP2}(Tz)/U_{corr}^{MP2}(Dz)] \quad (15)$$

Using eq 15 and X^{-3} scaling of correlation energy $U_{corr}^{MP2}(Xz)$ we find that the $U_{corr}^{MP4}(CBS)/U_{corr}^{MP2}(Dz)$ ratio is approximately 1.15 (±0.06) for minimum energy configurations from Figure 3. Similar results to those reported here were observed for small molecule dimers,[39,49] but much larger values of $U_{corr}^{MP4}(CBS)/U_{corr}^{MP2}(Dz)$ were reported for noble gases.[38]

The ϵ and r^* parameters (eq 13) were initially fitted to the MP2/aug-cc-pvDz dimer binding energies and then adjusted to yield the best fit to density, heat of vaporization, and self-diffusion coefficient of liquids, as shown in Table 2. Only a limited set of transferable repulsion−dispersion parameters was used and is given in Table 3. Compared to two-body force fields such as COMPASS,[4,5] our repulsion−dispersion parameters showed an improved transferability also reported for recent polarizable force fields by Kaminsky et al.[8] The dimer binding energies from MM calculations using the developed force field were most often between the MP2/aug-cc-pvTz and MP2/aug-cc-pvDz energies and somewhat lower than the MP2/CBS and MP4/CBS extrapolated energies, as shown in Figure 7 and Table 4. Figure 7 also indicates that the developed force field cannot describe dimer binding energy equally well along all paths. Abolishing combining rules and allowing the repulsion−dispersion parameters to be fitted independently resulted only in a marginal improvement of the fits to quantum chemistry binding energies, suggesting that the application of combining rules is not the main culprit of deviation of MM binding energies from the quantum chemistry data. Improvement of the electrostatic potential description by adding atomic (or bond) permanent dipoles may further improve ability of the force field to describe binding energetics along multiple path simultaneously; however, such improvements add significantly to computational expense of simulations.

D. Conformational Energetics. Relative conformational energies calculated at the MP2/aug-cc-pvDz//MP2/aug-cc-pvDz or MP2/aug-cc-pvDz//B3LYP/aug-cc-pvDz for DME, 1,2-DMP, 1−3 DMP, DMM, and DMC were used in fitting torsional parameters. The alkane torsional parameters were obtained by fitting conformational energetics from previous studies of hexane.[50] Bending and torsional parameters of fluoroalkanes were fit to C_5F_{12} and C_6F_{14}, as done in our previous work.[51]

The EC and PC O−C−C−O and GBL O−C−C−C− torsional parameters were obtained by fitting both the geometry of distorted optimized conformation and the energy of inversion through the planar conformation. The EC, PC, and GBL planar conformations were found to be 0.56, 0.60, and 1.64 kcal/mol higher, respectively, than the relaxed out-of-plain conformations, as determined at the MP2/aug-cc-pvDz//B3LYP/aug-cc-pvDz level. Supporting Information A summarizes conformational energetics of model compounds from the developed force field and quantum chemistry calculations.

IV. Molecular Dynamics Simulation Methodology

A polarizable version of the MD simulations code Lucretius[52] was used for all MD simulations. All systems were created in the gas phase with the initial periodic cell (box) size of 80−120 Å. The cell was shrunk in MD simulations using a Brownian dynamics algorithm[53] over a period of 0.3−5 ns to yield estimated liquid densities, with subsequent equilibration in the NPT ensemble for 0.2−0.5 ns for liquids and 2−4 ns for methoxy terminated PEO (MW = 2380), PPO (MW = 3124), PTMO (MW = 2369), and POM (MW = 2448). Table 2 summarizes lengths of production NPT runs performed after equilibrating runs. Production runs for polymers not listed in Table 2 (PEO (MW = 2380), PPO (MW = 3124), PTMO (MW = 2369), and POM (MW = 2448)) were 4−8 ns. Equilibrated periodic box lengths were from 27 to 40 Å. A Nose−Hoover thermostat[54] and a barostat[55] were used to control the temperature and pressure. Bond lengths were constrained using the Shake algorithm[56] to utilize a larger time step. The Ewald summation method was used for the treatment of long-range electrostatic forces between partial charges with partial charges and partial charges with induced dipoles for the many-body polarizable potential. Ewald parameters were $\alpha = 7-9$, $k_{limit} = 4-5$. A tapering function[57] was used to drive induced dipole−induced dipole interactions to zero at the cutoff of 10 Å, with scaling starting at 9 Å. A multiple time step reversible reference system propagator algorithm was employed,[58] with a time step of 0.5 fs for bonding, bending, and torsional motions, a 1.5 fs time step for nonbonded interactions within a 6.5 Å sphere, and a 3.0 fs time step for nonbonded interactions between 6.5 and 10.0 Å and the reciprocal space part of the Ewald summation.

MD simulations with intermolecular interactions turned off were performed for 0.3 ns using Brownian dynamics algorithm to calculate the gas-phase energy needed for the prediction of heat of vaporization. See Appendix eq. a1 for calculating the heat of vaporization from MD simulations.

V. Results and Discussion

A. Thermodynamic Properties. The densities and heats of vaporization for solvents from MD simulations and experiments are listed in Table 2. MD simulations yielded densities for liquids within 2% of experiment with the exception of acetone,

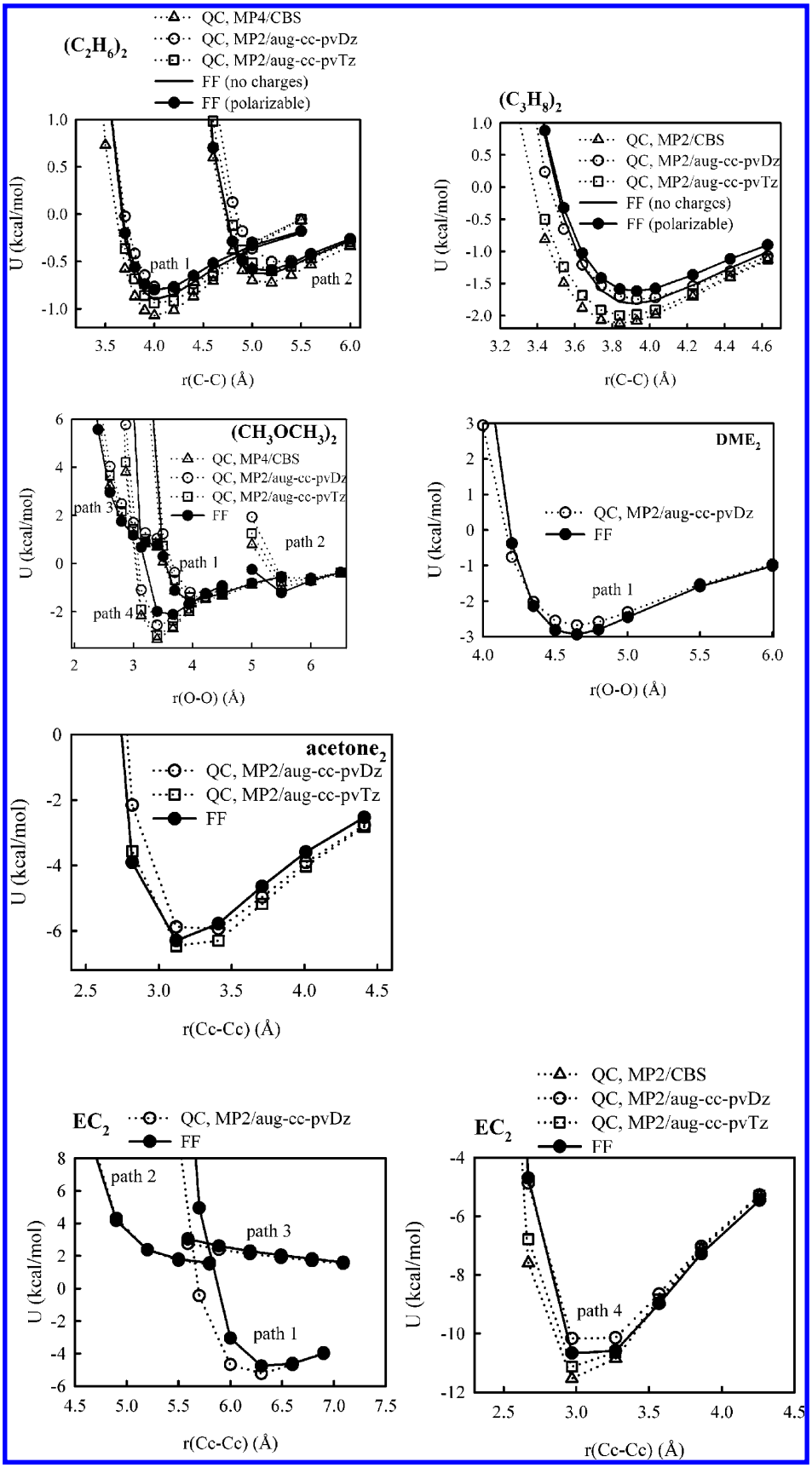

Figure 7. Dimer binding energies from quantum chemistry and MM using the developed force field. Nonpolarizable force field without charges was used in C_2H_6 and C_3H_8 dimer calculations.

which has the density predicted by MD simulations of 2.5% higher than the experimental value. Heats of vaporization were described with an average absolute error of 4% and a maximum error of 9%.

B. Structure. The static structure factor from MD simulations is compared with that from X-ray and neutron diffraction experiments in Figure 8 for alkanes, ethers, and carbonates. MD simulations predict a slightly higher magnitude of the first

TABLE 4: Separation Distances (Å) and Intermolecular Energies (kcal/mol) for the Dimer Lower-Energy Configurations from Quantum Chemistry and Force Field

dimer		MP4/CBS	MP2/CBS	MP2/Tz	MP2/Dz	PET-FF
$(C_2H_6)_2$ path 1	$r^{min}_{(C-C)}$	4.05	4.06	4.08	4.17	4.07
	U^{min}	−1.08	−1.01	−0.95	−0.82	−0.81
$(C_2H_6)_2$ path 2	$r^{min}_{(C-C)}$	5.15	5.20	5.23	5.29	5.13
	U^{min}	−0.73	−0.63	−0.60	−0.52	−0.60
$(C_3H_8)_2$ path 1	$r^{min}_{(C-C)}$		3.84	3.87	3.95	3.93
	U^{min}		−2.12	−2.00	−1.75	−1.62
(CH_3OCH_3)-path 1	$r^{min}_{(O-O)}$	4.14	4.17	4.19	4.23	4.12
	U^{min}	−1.78	−1.66	−1.61	−1.49	−1.68
(CH_3OCH_3)−path 4	$r^{min}_{(O-O)}$	3.41	3.44	3.46	3.50	3.59
	U^{min}	−3.46	−3.20	−3.04	−2.70	−2.14
DME_2−path 1	$r^{min}_{(O-O)}$				4.66	4.64
	U^{min}				−2.68	−2.94
EC_2−path 1	$r^{min}_{(Cc-Cc)}$				6.30	6.42
	U^{min}				−5.23	−4.93
EC_2−path 4	$r^{min}_{(Cc-Cc)}$		3.08	3.09	3.12	3.12
	U^{min}		−11.82	−11.52	−10.82	−11.39
$acetone_2$−path 1	$r^{min}_{(Cc-Cc)}$			3.25	3.27	3.21
	U^{min}			−6.75	−6.35	−6.44
average deviation from PET-FF	r^{min}	−0.04	−0.03	0.00	0.03	
	U^{min}	−0.45	−0.37	−0.26	0.02	
root mean-square deviation from PET-FF	r^{min}	0.09	0.08	0.07	0.09	
	U^{min}	0.68	0.52	0.40	0.31	

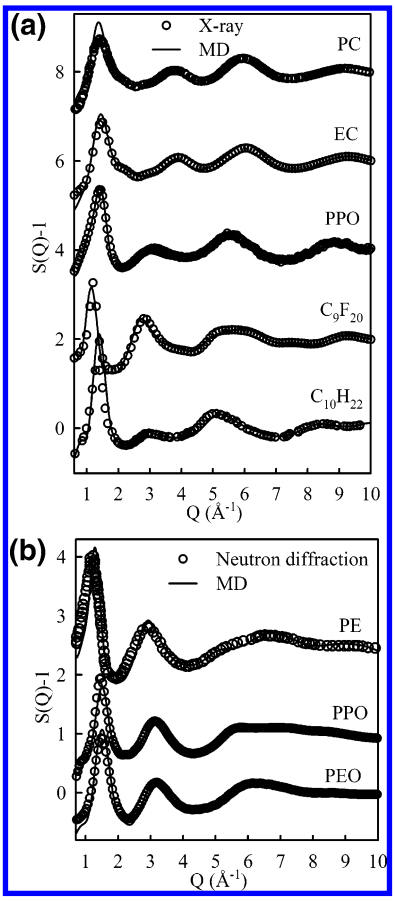

Figure 8. Static structure factor from MD simulations and X-ray experiments (a) for PPO[105] (300 K), $C_{10}H_{22}$[100] (298 K), PC and EC[101] (323 K), and C_9F_{20}[102] (295 K) and neutron diffraction experiments (b) for deuterated polyethylene[103] (440 K), PEO[104] (363 K), and PPO[105] (300 K).

amorphous peak of structure factor for $C_{10}H_{22}$ and PC compared to that of X-ray experiments. The deviation of MD results from X-ray data for $C_{10}H_{22}$ is rather puzzling because MD simulations predict the structure factor of polyethylene is good agreement with neutron diffraction experiments. Excellent agreement

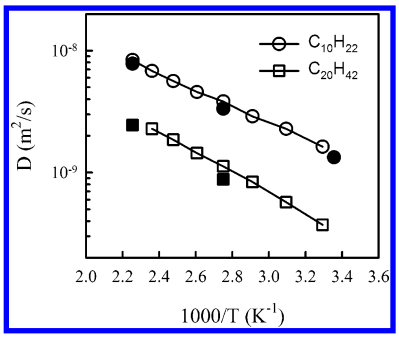

Figure 9. Self-diffusion coefficient of *n*-alkanes from NMR spin−echo measurements[106] and MD simulations.

between MD simulation predictions and diffraction experiments is observed for all other solvents shown in Figure 8.

C. Transport and Dynamic Properties. Self-diffusion coefficients of low molecular weight liquids from MD simulations are compared in Table 2 and Figure 9 with results of pgf-NMR measurements. The maximum deviation of MD-predicted self-diffusion coefficients from experiments was 30%, indicating a very good ability of our simulations to predict molecular diffusion. If self-diffusion coefficients are corrected for finite size effects as described in the Appendix, the quality of MD simulation predictions of self-diffusion coefficients becomes even better. The temperature dependence of the alkane self-diffusion coefficient is also accurately captured in MD simulations, as seen from Figure 9. The viscosities of selected liquids from MD simulations are compared with experiments in Table 5. An average deviation of 24% with the maximum deviation of 50% between MD simulation predictions of viscosity and experiments is observed.

Incoherent quasielastic neutron scattering (QNS) and neutron spin−echo experiments (NSE) of hydrogenated polymers probe hydrogen motion on various length and time scales. The length scale is probed in experiments by varying the magnitude of the momentum transfer vector (Q), which is typically $Q = 0.5-2.5$ Å^{-1}, allowing one to probe hydrogen motion at distances from 2.5 to 12 Å using $2\pi/Q$. The most direct comparison between experiment and simulations is achieved by comparing the intermediate scattering functions (ISF) $I(Q,t)$ obtained from

TABLE 5: Viscosity (μ) of Selected Liquids from MD Simulations and Experiments

liquid	T (K)	μ^{MD} (mPa s)	μ^{exp} (mPa s)	100% $(\mu^{MD-}\cdot\mu^{exp})/\mu^{exp}$	ref to exp data
DME	298	0.62	0.41	51	96
DMC	303	0.73	0.503	45	97
EC	313	1.9	1.85	3	82
PC	303	2.5	2.3	9	96
GBL	303	1.3	1.612	−19	93
acetone	298	0.32	0.306	5	98
C_5F_{12}	298	0.55	0.66	−17	99

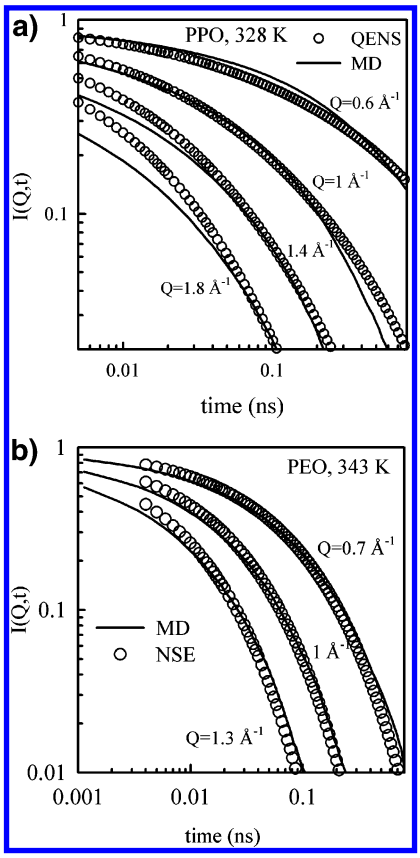

Figure 10. Intermediate incoherent structure factor of PPO[105] at 328 K and PEO at 343 K from MD simulations, QNS, and NSE experiments. Fits to experimental data are shown.

the QNS experiment with those calculated from the MD simulations. As scattering from hydrogen is the dominant contribution and it is essentially entirely incoherent scattering, only the incoherent ISF is relevant. The ISF's from MD simulations are compared with those from QNS[59] and NSE[60] experiments for PEO and PPO in Figure 10. Good agreement is observed between ISF predicted by MD simulations and QENS and NSE experiments, with MD simulations predicting slightly slower relaxation at long times and slightly faster relaxation at short times.

The ^{13}C NMR spin−lattice relaxation times (T_1) probe the rate of decay of the C−H vector, which is related to polymer dynamics. MD simulations predicted PEO T_1 ^{13}C spin−lattice relaxation times within 30% of those measured in recent NMR experiments,[18] as demonstrated in Table 6. Slightly slower dynamics of interior carbons from MD simulations, as reflected by higher T_1 values, is consistent with the slightly slower relaxation of PEO as probed by ISF from NSE experiments. We note that PEO dynamic properties from the developed force field are in better agreement with experimental data compared to predictions using the previous PEO force field.[18]

TABLE 6: ^{13}C Spin−Lattice Relaxation Times (T_1) from MD Simulations of PEO (MW = 2380) and NMR Experiments of PEO (MW = 1854); Carbon Types Are Defined as Following: $C^{methyl}H_3-O-C^{\alpha}H_2-C^{\beta}H_2-O-C^{interior}H_2-\cdots$

carbon type	T_1(s) MD	T_1(s) NMR	relative deviation (%) $100\%(T_1^{MD}-T_1^{NMR})/T_1^{NMR}$
interior	0.96	1.26	24
b	1.64	2.09	22
a	2.63	3.18	17
methyl	9.34	8.74	−7
interior	1.17	1.66	30
b	2.10	2.85	26
a	3.63	4.38	17
methyl	11.74	10.77	−9

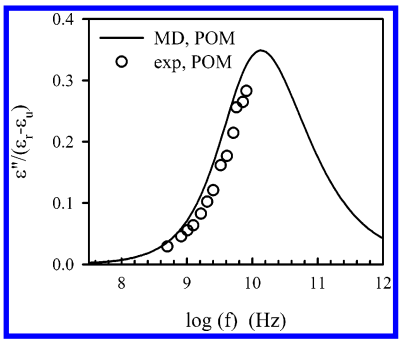

Figure 11. Dielectric loss of POM from MD simulations and dielectric relaxation experiments at 465 K.

The ability of the developed force field to accurately predict POM conformational dynamics was investigated by comparing frequency dependent dielectric relaxation predicted by MD simulations with experiments,[61,62] as shown in Figure 11. An excellent agreement between simulation predictions and experiments is found for the range where experimental data are available.

VI. Conclusions

Many-body polarizable force fields were developed for common liquid and polymer solvents with potential usage in Li-batteries. Only a few repulsion−dispersion parameter types (C, H, O, F, N, C_m (methoxy carbon), and C_c (carbonyl carbon)) were needed to provide a good description/prediction of solvent heats of vaporizations, densities, self-diffusion coefficients, structure factors, and conformational dynamics of solvents. Gas-phase dimer binding energies from molecular mechanics calculations using a developed force field were typically between MP2/aug-cc-pvDz and MP2/aug-cc-pvTz energies from quantum chemistry calculations and less than the complete basis set extrapolated dimer energies calculated at both MP2 and MP4 levels.

Acknowledgment. We are indebted to subcontract from LBL #6515401 and NASA (Grant NAG3 2624) for financial support.

Appendix

Property Calculation from MD Simulations. *1. Enthalpy of Vaporization.* Heats of vaporization (ΔH) are calculated using eq a1

$$\Delta H = U^{liq} - U^{vap} + RT \qquad \text{(a1)}$$

where U^{liq} and U^{vap} are the energies of liquid and gas phases,

R is the gas constant, and T is the temperature. The gas-phase energy is calculated in MD simulations using Brownian dynamics and no nonbonded interaction between molecules.

2. Static Structure Factor. The static structure factor is calculated using eq a2

$$S(Q) = 1 + \frac{1}{\langle b\rangle^2} n \sum_{\alpha\beta} x_\alpha b_\alpha x_\beta b_\beta \int_0^{r_c} [g_{\alpha\beta}(r) - 1] \frac{\sin Qr}{Qr} 4\pi r^2 dr \quad \text{(a2)}$$

where $\langle b\rangle^2 \equiv \sum_\alpha x_\alpha x_\beta b_\alpha b_\beta$, n is a number density, $g_{\alpha\beta}(r)$ is the radial distribution function (RDF) for $\alpha\beta$ atom types, Q is the wave vector, b_α is the coherent scattering length for species α, x_α is a fraction of atom type α, and r_c is the cutoff for integration equal to half of the simulations box.

3. Intermediate Incoherent Dynamic Structure Factor. For isotropic systems such as liquids, the neutron scattering incoherent intermediate scattering function (ISF), $I(Q,t)$, is given by eq a3[63]

$$I_{inc}(Q,t) = \left\langle \frac{\sin(\Delta r_i(t)Q)}{\Delta r_i(t)Q} \right\rangle \quad \text{(a3)}$$

where $\Delta r_i(t)$ is the displacement of atom i after time t, Q is the magnitude of the momentum transfer vector, and $\langle\ \rangle$ denotes an average over-all time origin for atoms with a significant incoherent cross section (i.e., hydrogen atoms).

4. Frequency-Dependent Dielectric Constant. Linear response theory allows us to obtain the complex dielectric permittivity $\epsilon^*(\omega) = \epsilon' + i\epsilon''$ for the PEO melt using the relationship[64]

$$\frac{\epsilon' + i\epsilon}{\Delta\epsilon} = 1 - i\omega \int_0^\infty \Phi(t)\exp(-i\omega t)dt \quad \text{(a4)}$$

where the dipole moment autocorrelation function (DACF) is given by

$$\Phi(t) = \frac{\langle \boldsymbol{M}(0)\cdot\boldsymbol{M}(t)\rangle}{\langle \boldsymbol{M}(0)\cdot\boldsymbol{M}(0)\rangle} \quad \text{(a5)}$$

where $\Delta\epsilon$ relaxation strength is equal to ϵ_r - ϵ_u. Here, $\boldsymbol{M}(t)$ is the dipole moment of the system at time t, V is the volume of the system, k_B is the Boltzmann constant, T is the temperature, and $\langle\ \rangle$ denotes an ensemble average. The unrelaxed dielectric constant ϵ_u is the dielectric constant that includes all relaxation processes at frequencies higher than the process of interest, i.e., electronic polarization and relaxation due to vibrations and librations, whereas the relaxed dielectric constant ϵ_r is the value obtained after the relaxation process, i.e., dipole orientational relaxation, is complete.

5. NMR Spin−Lattice Relaxation Times T_1. The experimentally determined T_1 values are related to the microscopic motion of the C−H vectors through the relationships[65]

$$\frac{1}{nT_1} = K[J(\omega_H - \omega_C) + 3J(\omega_C) + 6J(\omega_H + \omega_C)] \quad \text{(a6)}$$

where n is the number of attached protons, ω_C and ω_H are the Larmor (angular) frequencies of the ^{13}C and ^1H nuclei, respectively, and γ_C and γ_H are the corresponding gyromagnetic ratios. The constant K is given by[65]

$$K = \frac{\hbar^2 {\mu_0}^2 {\gamma_H}^2 \gamma C^2 \langle {r_{CH}}^{-3}\rangle^2}{160\pi^2} \quad \text{(a7)}$$

where μ_0 is the permittivity of free space and r_{CH} is the carbon−hydrogen bond length. K assumes values of $2.29 \times 10^9\ s^{-2}$ for sp^3 hybridized nuclei.[65] The spectral density function $J(\omega)$ is given as[65]

$$J(\omega) = \frac{1}{2}\int_{-\infty}^{\infty} P_2^{CH}(t)\ e^{i\omega t} dt \quad \text{(a8)}$$

where

$$P_2^{CH}(i,t) = \frac{1}{2}\{3\langle[\mathbf{e}_{CH}(i,t)\cdot\mathbf{e}_{CH}(i,0)]^2\rangle - 1\} \quad \text{(a9)}$$

Here, $\mathbf{e}_{CH}$ is a unit vector along a particular C−H bond, and the index i denotes differentiable resonances due to the local environment (methyl, α,β, interior carbons).

6. Self-Diffusion Coefficient. Self-diffusion coefficient D is calculated using Einstein relation,

$$D = \lim_{t\to\infty} \frac{\langle R^2(t)\rangle}{6t} \quad \text{(a10)}$$

where $R^2(t)$ is mean-square displacement of a molecule center of mass during time t, and $\langle\ \rangle$ denotes an ensemble average.

Due to finite size of the simulation cell, long-range hydrodynamic interactions restrict diffusion of species. The leading order of finite size correction to self-diffusion coefficient (ΔD^{FSC}) was found to be linearly proportional to the simulation box and is given by eq a11,[66]

$$\Delta D^{FSC} = \frac{2.837 k_B T}{6\pi\eta L} \quad \text{(a11)}$$

where k_B is the Boltzmann constant, T is temperature, L is a linear dimension of the simulation periodic cell, and η is viscosity.

7. Viscosity. The viscosity is calculated using the Einstein relation[67]

$$\eta = \lim_{t\to\infty} \frac{V}{6k_B T t}\left\langle\left\langle \sum_{\alpha>\beta} (L_{\alpha\beta}(t) - L_{\alpha\beta}(0))^2 \right\rangle\right\rangle \quad \text{(a12)}$$

where

$$L_{\alpha\beta}(t) = \int_0^t P_{\alpha\beta}(t')dt'$$

k_B is the Boltzmann constant, T is temperature, t is time, $P_{\alpha\beta}$ is the symmeterized stress sensor, and V is the volume of the simulation box.

Supporting Information Available: A summary of conformational energetics from quantum chemistry calculations and developed force field is included in Supporting Information A. Developed force field parameters for solvents and their interaction with LiTFSI are listed in Supporting Information B. This material is available free of charge via the Internet at http://pubs.acs.org.

References and Notes

(1) Cornell, W. D. et al. *J. Am. Chem. Soc.* **1995**, *117*, 5179.
(2) Wang, J.; Ceiplak, P.; Kollman, P. *J. Comput. Chem.* **2000**, *21*, 1049.
(3) Cieplak, P.; Caldwell, J.; Kollman, P. *J. Comput. Chem.* **2001**, *22*, 1048.
(4) Sun, H. *J. Phys. Chem. B* **1998**, *102*, 7338.
(5) Rigby, D.; Sun, H.; Eichinger, B. E. *Polym. Int.* **1997**, *44*, 311.
(6) Jorgensen, W. L.; Maxwell, D. S.; Tirado-Rives, J. *J. Am. Chem. Soc.* **1996**, *118*, 11225.
(7) MacKerell, A. D. et al. *J. Phys. Chem. B* **1998**, *102*, 3586.

(8) Kaminski, G. A.; Stern, H. A.; Berne, B. J.; Friesner, R. A.; Cao, Y. X.; Murphy, R. B.; Zhou, R.; Hangren, T. A. *J. Comput. Chem*. **2002**, *23*, 1515.
(9) Patel, S.; Brooks. C. L. *J. Comput. Chem*. **2004**, *25*, 1.
(10) Kaminski, G. A.; Stern, H. A.; Berne, B. J.; Friesner, R. A. *J. Phys. Chem. A.* **2004**, *108*, 621−627.
(11) Mayo, S. L.; Olafson, B. D.; Goddard, W. A., III. *J. Phys. Chem.* **1990**, *94*, 8897.
(12) Rappé, A. K.; Casewit, C. J.; Colwell, K. S.; Goddard, W. A.; Skiff, W. M. *J. Am. Chem. Soc.* **1992**, *114*, 10024.
(13) Ren, P.; Ponder, J. W. *J. Phys. Chem. B* **2003**, *107*, 5933.
(14) Jorgensen, W.; Chandrasekhar, J.; Madura, J. D.; Impey, R. W.; Klein, M. L. *J. Chem. Phys.* **1983**, *79*, 926.
(15) Berendsen, H. J. C.; Grigera, J. R.; Straatsma, T. P. *J. Phys. Chem.* **1987**, *91*, 6269.
(16) Smith, G. D.; Bedrov, D.; Byutner, O.; Borodin, O.; Sewell, T. D. *J. Phys. Chem. A* **2003**, *107*, 7552.
(17) Smith, G. D.; Borodin, O.; Bedrov, D. *J. Comput. Chem*. **2002**, *23*, 1480.
(18) Borodin, O.; Smith, G. D.; Douglas, R. *J. Phys. Chem. B* **2003**, *107*, 6824.
(19) Borodin, O.; Smith, G. D. Molecular Modeling of Poly(Ethylene Oxide) Melts And Poly(Ethylene Oxide)-Based Polymer Electrolytes. In *Methods and Applications in Computational Materials Chemistry*; Curtiss, L., Gordon, M., Eds.; Kluwer Academic Publishers: Boston, MA, 2004; pp 35−90.
(20) Allen, W.; Rowley, R. L. *J. Chem. Phys.* **1997**, *106*, 10273.
(21) McCabe, C.; Bedrov, D.; Borodin, O.; Smith, G. D.; Cummings, P. T. *Ind. Eng. Chem. Res.* **2003**, *42*, 6956−6961.
(22) Bornder, A. J.; Cavasotto, C. N.; Abagyan, R. A. *J. Phys. Chem. B* **2003**, *107*, 9601.
(23) Kaminski, G.; Jorgensen, W. L. *J. Phys. Chem.* **1996**, *100*, 18010−18013.
(24) Borodin, O.; Bell, R. L.; Li, Y.; Bedrov, D.; Smith, G. D. *Chem. Phys. Lett.* **2001**, *336*, 292−302.
(25) Tasaki, K. *J. Electrochem. Soc*. **2002**, *149*, A418.
(26) Borodin, O.; Smith, G. D.; Jaffe, R. L. *J. Comput. Chem.* **2001**, *22*, 641−654.
(27) Borodin, O.; Smith, G. D. *J. Phys. Chem. B* **2003**, *107*, 6801.
(28) Spangberg, D.; Hermansson, K. *J. Chem. Phys.* **2004**, *120*, 4829−4843.
(29) Grossfield, A.; Ren, P.; Ponder, J. W. *J. Am. Chem. Soc* **2003**, *125*, 15671−15682.
(30) Bukowski, R.; Szalewicz, K.; Chabalowski, *J. Phys. Chem. A* **1999**, *103*, 7322.
(31) Polyoxymethylene oxide does not dissolve Li-salts and, therefore, is not used as a electrolyte by itself,; however, oxymethylene spacers are often used in poly(ethylene oxide) to prevent crystallization of the later.
(32) Stern, H. A.; Kaminski, G. A.; Banks, J. A.; Zhou, R.; Berne, B. J.; Friesner, R. A. *J. Phys. Chem. B* **1999**, *103*, 4730−4737.
(33) Masia, M.; Probst, M.; Rey, R. *J. Chem. Phys.* **2004**, *121*, 7362−7378.
(34) Borodin, O.; Smith, G. D. *J. Phys. Chem*. **2006**, 10.
(35) Positioning the "extended charge" at 0.5 Å from the oxygen atom yielded the best description of the electrostatic potential around dimethyl ether.
(36) Thole, B. T. *Chem. Phys.* **1981**, *59*, 341.
(37) Ren, P.; Ponders, J. W. *J. Phys. Chem. B* **2003**, *107*, 5933−5947.
(38) Woon, D. E. *J. Chem. Phys.* **1994**, *100*, 2838−2850.
(39) Rowley, R. L.; Yang, Y.; Pakkanen, T. A. *J. Chem. Phys.* **2001**, *114*, 6058−6067.
(40) Al-Matar, A.; Rockstraw D. A. *J. Comput. Chem*. **2004**, *25*, 660.
(41) Song, W.; Rossky, P. L.; Maroncelli, M. *J. Chem. Phys.* **2003**, *119*, 9145.
(42) Ewig, C. S.; Thacher, T. S.; Hagler, A. T. *J. Phys. Chem. B* **1999**, *103*, 6998.
(43) Waldman, M.; Hagler A. T. *J. Comput. Chem.* **1993**, *14*, 1077.
(44) Frisch, M. J.; Trucks, G. W.; Schlegel, H. B.; Scuseria, G. E.; Robb, M. A.; Cheeseman, J. R.; Zakrzewski, V. G.; Montgomery, J. A., Jr.; Stratmann, R. E.; Burant, J. C.; Dapprich, S.; Millam, J. M.; Daniels, A. D.; Kudin, K. N.; Strain, M. C.; Farkas, O.; Tomasi, J.; Barone, V.; Cossi, M.; Cammi, R.; Mennucci, B.; Pomelli, C.; Adamo, C.; Clifford, S.; Ochterski, J.; Petersson, G. A.; Ayala, P. Y.; Cui, Q.; Morokuma, K.; Malick, D. K.; Rabuck, A. D.; Raghavachari, K.; Foresman, J. B.; Cioslowski, J.; Ortiz, J. V.; Stefanov, B. B.; Liu, G.; Liashenko, A.; Piskorz, P.; Komaromi, I.; Gomperts, R.; Martin, R. L.; Fox, D. J.; Keith, T.; Al-Laham, M. A.; Peng, C. Y.; Nanayakkara, A.; Gonzalez, C.; Challacombe, M.; Gill, P. M. W.; Johnson, B. G.; Chen, W.; Wong, M. W.; Andres, J. L.; Head-Gordon, M.; Replogle, E. S.; Pople, J. A. *Gaussian 98*, revision A.1; Gaussian, Inc.: Pittsburgh, PA, 1998.
(45) Anisimov, V. M.; Lamoureux, G.; Vorobyov, I. V.; Huang, N.; Roux, B.; MacKerell, A. D. *J. Chem. Theory Comput.* **2005**, *1*, 153.
(46) Halkier, A.; Klopper, W.; Helgaker, T.; Jørgensen, P.; Taylor, P. R. *J. Chem. Phys.* **1999**, *111*, 9157.
(47) Smith, G. D.; Borodin, O.; Bedrov, D. *J. Comput. Chem*. **2002**, *23*, 1480−1488.
(48) Klauda, J. B.; Garrison, S. L.; Jiang, J.; Arora, G.; Sandler, S. I. *J. Phys. Chem. A* **2004** *108*, 107−112.
(49) Tsuzuki, S.; Uchimaru, T.; Mikami, M.; Tanabe, K. *J. Phys. Chem. A.* **2002**, *106*, 3867−3872.
(50) Smith, G. D.; Jaffe, R. L. *J. Phys. Chem.* **1996**, *100*, 18718.
(51) Borodin, O.; Smith, G. D.; Bedrov, D. *J. Phys. Chem. B* **2002**, *106*, 9912.
(52) Lucretius, www.che.utah.edu/∼gdsmith.
(53) Smith, G. D.; Jaffe, R.; Yoon, D. Y. *Macromolecules* **1993**, *26*, 298.
(54) Nose, S. In *Computer Simulation in Materials Science*; Meyer, M., Pontikis, V., Eds.; Kluwer Academic Publishers: Netherlands, 1991; p 21.
(55) Martyna, G. J.; Tuckerman, M.; Tobias, D. J.; Klein, M. L. *Mol. Phys.* **1996**, *87*, 1117.
(56) Ryckaert, J. P.; Ciccotti, G.; Berendsen, H. J. C. *J. Comput. Phys.* **1977**, *23*, 327.
(57) Steinhauser, O. *Mol. Phys.* **1982**, *45*, 335.
(58) Martyna, G. J.; Tuckerman, M.; Tobias, D. J.; Klein, M. L. *Mol. Phys.* **1996**, *87*, 1117.
(59) Mos, B.; Verkerk, P.; Pouget, S.; van Zon, A.; Bel, G.-J.; de Leeuw, S. W.; Eisenback, C. D. *J. Chem. Phys.* **2000**, *113*, 4.
(60) Andersson, D.; Carlsson, P.; Engberg, D.; Torell, L. M.; Börjesson, L.; McGreevy, R. L.; Howells, W. S. *Physica B* **1999**, *266*, 126.
(61) Porter, C. H.; Boyd, R. H. *Macromolecules* **1971**, *4*, 589.
(62) Porter, C. H.; Lawler, J. H. L.; Boyd, R. H. *Macromolecules* **1971**, *3*, 308−314.
(63) Higgins, J. S.; Benoît, H. C. *Polymers and Neutron Scattering*; Clerendon Press: Oxford, 1996.
(64) Edwards, D. M. F.; Madden, P. A.; McDonald, I. R. *Mol. Phys.* **1984**, *51*, 1141.
(65) Gisser, D. J.; Glowinkowski, S.; Ediger, M. D. *Macromolecules* **1991**, *24*, 4270.
(66) Dünweg, B.; Kremer, K. *J. Chem. Phys.* **1993**, *99*, 6983.
(67) Haile, J. M. *Molecular Dynamics Simulations*; Wiley: New York, 1992.
(68) *Physical Property Data for the Design Engineer*; Beaton, C. F., Hewitt, G. F., Eds.; Hemisphere Publishing Co.: New York, 1989.
(69) Witt, R. K.; Kemp, J. D. *J. Am. Chem. Soc*. **1937**, *59*, 273−276.
(70) Greiner-Schmid, A.; Wappmann, S.; Has, M.; Lüdemann, H.-D. *J. Chem. Phys*. **1991**, *94*, 5643.
(71) Majer, V.; Svoboda, V. *Enthalpies of Vaporization of Organic Compounds: A Critical Review and Data Compilation*; Blackwell Scientific Publications: Oxford, 1985; p 300.
(72) Cibulka, I.; Hnedkovsky, L. *J. Chem. Eng. Data* **1996**, *41*, 657−668.
(73) Fishman, E. *J. Phys. Chem.* **1955**, *59*, 469.
(74) CRC Handbook of Chemistry and Physics, 85th edition, 2004−2005. http://www.hbcpnetbase.com/.
(75) Mondello, M.; Grest, G. S. *J. Chem. Phys.* **1997**, *106*, 9327.
(76) *Physical Property Data for the Design Engineer*; Beaton, C. F., Hewitt, G. F., Eds.; Hemisphere Publishing Co.: New York, 1989.
(77) Witt, R. K.; Kemp, J. D. *J. Am. Chem. Soc*. **1937**, *59*, 273−276.
(78) Greiner-Schmid, A.; Wappmann, S.; Has, M.; Lüdemann, H.-D. *J. Chem. Phys*. **1991**, *94*, 5643.
(79) Wu, J.; Liu, Z.; Bi, S.; Meng, X. *J. Chem. Eng. Data* **2003**, *48*, 426.
(80) Heinrich-Schramm, A.; Price, W. E.; Lüdemann, H.-D. *Natruforsch Z.* **1995**, *50*, 145.
(81) Ku, H.-S.; Tu, C.-H. *J. Chem. Eng. Data* **2000**, *45*, 391.
(82) Hayamizu, K.; Aihara, Y.; Arai, S.; Martinez, C. G. *J. Phys. Chem. B* **1999**, *103*, 519.
(83) Pal, A.; Kumar, H. *J. Chem. Eng. Data* **1999**, *44*, 1330.
(84) Lide, D. R. *Handbook of Organic Solvents*; CRC Press: Boca Raton, FL, 1995.
(85) Flick, E. W. *Industrial Solvent Handbook*, 2nd edition; Noyes Data Corporation: Park Ridge, NY, 1998.
(86) Francesconi, R.; Comelli, F. *J. Chem. Eng. Data* **1995**, *40*, 512.
(87) McEachern, D. M., Jr.; Kilpatrick, J. E. *Ber. Bunsen-Ges. Phys. Chem*. **1964**, *41*, 3127.
(88) Lai, C.-C. M. S. Thesis, University of Utah, 1970.
(89) Tasieć, A.; Djordjević, B. D.; Šerbanović, S. P.; Grozdanić, D. K. *J. Chem. Eng. Data* **1981**, *26*, 118.
(90) Hong, C. S.; Waksiak, R.; Finston, H.; Fried, V. *J. Chem. Eng. Data* **1982**, *27*, 146.
(91) Wankhede, D. S.; Lande, M. K.; Arbad, B. R. *J. Chem. Eng. Data* **2005**, *50*, 261.
(92) Steele, W. V.; Chirico, R. D.; Knipmeyer, S. E.; Nguyen, A. *J. Chem. Eng. Data*. **1997**, *42*, 1008.

(93) Moumouzias, G.; Ritzoulis, C.; Ritzoulis, G. *J. Chem. Eng. Data*, **1999**, *44*, 1187−1191.
(94) Steele, W. V.; Chirico, R. D.; Nguyen, A.; Hossenlopp, I. A.; *AIChE Symp. Ser.* **1989**, *85*, 140.
(95) Yang, J.; Ren, Y.; Tian, A.; Sun, H. *J. Phys. Chem. B* **2000**, *104*, 4951.
(96) Barthel, J.; Neueder, R.; Roch, H. *J. Chem. Eng. Data* **2000**, *45*, 1007−1011.
(97) Aminabhavi, T. M.; Kamalika, B. *J. Chem. Eng. Data* **1998**, *43*, 1096−1101.
(98) Agarwal, D.; Singh, M. *J. Chem. Eng. Data* **2004**, *49*, 1218−1224.
(99) Harkins, D. *Evaluation of Available Perfluorobutane Data for Selected Physical Properties*; Oak Ridge Gaseous Diffusion Plant, 1990.
(100) Habenschuss, A; Narten, A. N. *J. Chem. Phys.* **1990**, *92*, 5692−5699.
(101) Soetens, J.-C.; Millot, C.; Maigret, B.; Bakó, I. *J. Mol. Liq.* **2001**, *92*, 5692−5699.
(102) Borodin, O.; Smith, G.D.; Bedrov, D. *J. Phys. Chem. B* **2002**, *106*, 9912−9922.
(103) Misawa, M.; Kanaya, T.; Furunaga, T. *J. Chem. Phys.* **1991**, *94*, 8413.
(104) Annis, B. K.; Borodin, O.; Smith, G. D.; Benmore, C.; Soper, A. K.; Londono, J. D. *J. Chem. Phys.* **2001**, *115*, 10998.
(105) Ahlstrom, P.; Borodin, O.; Wahnström, G.; Wensink, E.; Smith, G. D.; Carlsson, P. *J. Chem. Phys.* **2000**, *112*, 10669−10679.
(106) Meerwall, E.; Beckman, S.; Jang, J.; Mattice, W. L. *J. Chem. Phys.* **1999**, *108*, 4299.